



ORIGINAL ARTICLE

Aerodynamic performance of the dragonfly wing section in gliding mode at ultra-low Reynold number

Sarvesh Kumar, Husain Mehdi, Piyush Gupta

Department of Mechanical Engineering, Meerut Institute of Engineering and Technology, Meerut, India.

Article Information

Received: 07 June 2022
Revised: 21 Aug 2022
Accepted: 29 Aug 2022
Available online: 04 Sep 2022

Keywords:

Pressure contour
Vortex formation
Reynolds Number
Angle of attack

Abstract

The CFD simulation of fluid flow and aerodynamic performance of the dragonfly (*Aeshna Cyanea*) wing section was examined using FLUENT software at low Reynolds numbers (1000, 1250, and 1500) with various angles of attack (AOA) (0° , 5° , 10°). The numerical solver was based on the SIMPLE algorithm with Green-Gauss Node velocity pressure coupling. With increasing AOA, the mean lift coefficient increased while the drag coefficient decreased, resulting in improved propulsive performance. As the AOA rises, the gliding ratio increases in lockstep. The drag formation has some exciting outcomes. Because viscous effects are more significant at lower Re values, leading skin friction to be the primary contributor to drag reduction, the average drag coefficient in each case drops as the AOA increases.

©2022 ijrei.com. All rights reserved

1. Introduction

In recent years, the concept of micro-sized micro air vehicles (MAVs) with the primary surveillance function has increased. MAVs are typically small planes with a maximum span of 150 mm and a top speed of 10 m/sec [1-3]. The flight regime has an extraordinarily low Re-number due to the small span scale and fast flight speed. The Defense Advanced Research Project Agency (DARPA) (MAVs) first developed Micro Air Vehicles. These aren't miniature copies of bigger planes. They are in a class by themselves in terms of price, functionality, and military capability. Flapping foils are being researched for use in MAVs and autonomous underwater vehicles as a source of lift (AUVs). Perceiving insects, birds, and insects can teach us about the fluid dynamics of these biologically excited flows. Their utility is limited by the absence of experimental studies of flapping foil in nature capable of obtaining full-field regionally determined pressure and velocity measurements [4].

The requirement to work with live creatures dictates the specific settings, as it is challenging to forecast the actions of these insects/birds during testing conditions.

Furthermore, in a structure like an insect's/flapping bird's wings, there is no mechanism for extracting shear stress and surface pressure distribution [5]. *Pantala flavescens* can fly for 10-15 seconds at around 15 m/s. Dragonflies of the *Aeshna* genus can glide for up to 30 seconds without losing altitude [6]. A smaller dragonfly was filmed with a glide time of 0.5 seconds, a span of 1 m, and a gliding speed of 2.5 meters per second. The typical Reynolds number (Re) range in gliding flight is 10^2 and 10^4 [7-10]. As a result, this fluid flow is called an ultra-low Reynolds number regime. The dragonfly is no exception for producing lift; its forewings should flap. The usual flapping frequency of an airfoil in forwarding flight is between 24 and 30 Hz [11, 12]. *Aeshna Cyanea*, on the other hand, could be classified as gliders because they frequently cover four-chord spans in a single wing beat [13]. Furthermore,

Corresponding author: Sarvesh Kumar

Email Address: spp24212@gmail.com

<https://doi.org/10.36037/IJREI.2022.6504>

as the ambient temperature rises, the frequency of wing beats lowers. At the same time, the duration of gliding increases [14], and it was proposed that the airfoil adopt this gliding style to profit from cooling convection in the hot climate.

The thoracic flight muscles responsible for heat production may relax in the dragonfly, allowing it to glide with little effort [15-17].

We investigate the fluid flow and aerodynamic performance of a sliced part of a dragonfly airfoil with varied angles of attack (AOA) ranging from 0° to 10° in this paper.

According to the author's best knowledge, the aerodynamic performance at such a low Re number has yet to be investigated. These parameter ranges apply to both dragonflies and MAVs. The intermediate cross-section of a dragonfly wing is represented by the pleated airfoil used in the simulation. In Fig. 1, profile 2 [3] was chosen for numerical simulation.



Figure 1: Pleated cross-section of dragonfly wing section [3]

2. Governing equations

The incompressible Navier-Stock equations were discretized using a finite volume technique, and the solution uses a time-dependent, standard form. The incompressible Navier-Stock equations are written in a tensor form as:

$$\frac{\partial u_i}{\partial x_i} = 0 \tag{1}$$

$$\frac{\partial u_i}{\partial t} + \frac{\partial(u_i u_j)}{\partial x_j} = -\frac{1}{\rho} \frac{\partial p}{\partial x_i} + \nu \frac{\partial}{\partial x_j} \left(\frac{\partial u_i}{\partial x_j} \right) \tag{2}$$

The Navier stokes equations were derived with the help of cell centred, non-staggered layout, and eq. 2 may be written as

$$\frac{\partial u_i}{\partial t} + \frac{\partial(u_i u_j)}{\partial x_j} = -\frac{\partial p}{\partial x_i} + \frac{1}{Re} \frac{\partial^2 u_i}{\partial x_j \partial x_j} \tag{3}$$

$$\frac{\partial u_i}{\partial x_i} = 0 \tag{4}$$

$$Re = \frac{\rho U_0 c}{\mu}$$

Where i is 1, 2 and 3 in the x, y, and z direction, while velocity component represented as $u_1, u_2,$ and u_3 corresponding to u, v, and w respectively. μ and ρ are dynamic viscosity and density of the fluid. The above equations are non dimensionalized using the relevant velocity and length scales. Re, c, u_0 are Reynolds number, chord length of airfoil, and streamline velocity. A pressure-based solution was used to investigate equation 3. This strategy employs a prediction method algorithm [18]. In the projection approach, the mass

conservation requirement of the velocity field was addressed by solving a pressure equation. The pressure equation was generated using the continuity and momentum equations and adjusted velocity fields. The governing equation was nonlinear, and the solution strategy included iterations in which the entire set of governing equations was solved simultaneously until the solution converged. The pressure solver solves the governing equation with a solution approach.

2.1 General Scalar Transport Equation Discretization and Solution

This method uses control volume to convert a scalar equation into a numerically solvable equation that may be used to solve conservation equations for carrying a scalar quantity (ϕ). The integration of the transport equation through each boundary condition leads to a discrete equation that describes the conversion rule on a control volume basis, as illustrated below.

$$\iiint \frac{\partial \rho \phi}{\partial t} dV + \oint \rho \phi \vec{v} \cdot d\vec{A} = \oint \Gamma_\phi \nabla \phi \cdot d\vec{A} + \iiint S_\phi dV \tag{5}$$

Where, $S_\phi, \nabla_\phi, \Gamma_\phi, \vec{A}, \vec{v}$, and ρ are source of ϕ per unit volume, ϕ gradient, diffusion coefficient of ϕ , surface vector, velocity vector, and density respectively. The discretization of equation 5 on a given cell may be written as

$$\frac{\partial \rho \phi}{\partial t} V + \sum_f^{N_{faces}} \rho_f \vec{v}_f \phi_f \cdot \vec{A}_f = \sum_f^{N_{faces}} \Gamma_\phi \nabla \phi_f \cdot \vec{A}_f + S_\phi V \tag{6}$$

The 2nd order upwind approach is used to discretize the momentum equation. When the 2nd order upwind was applied, numbers at cell faces were detected using a multivariate linear equation [19]. This method used the Taylor series extension to obtain higher-order precision at cell faces. The face value was determined as follows when the 2nd order up-wind was used:

$$\phi_{f,sou} = \nabla \phi \cdot \vec{r} + \phi \tag{7}$$

Where \vec{r} is the displacement vector, and $\nabla \phi$ is gradient. In this work, Green-Gauss Node based method, $\nabla \phi$ may be calculated as follow:

$$\bar{\phi}_f = \frac{1}{N_f} \sum_n^{N_f} \bar{\phi}_n \tag{8}$$

Where N_f = Number of nodes

The node value was calculated using the cell values around the nodes [20, 21]. The cell-based gradient method is quite similar to the node-based gradient method for unstructured or irregular models. The following is how the continuity and momentum equations can be discretized.

$$\oint \rho \vec{v} \cdot d\vec{A} = 0 \tag{9}$$

$$\oint \rho \vec{v} \cdot d\vec{A} = -\oint p I \cdot d\vec{A} + \oint \vec{\tau} \cdot d\vec{A} + \iiint \vec{F} dV \quad (10)$$

$$a_p u = \sum_{nb} a_{nb} u_{nb} + \sum p_f A \cdot \vec{i} + S \quad (11)$$

$$\sum_f^{N_{faces}} J_f A_f = 0 \quad (12)$$

$$J_f = \rho_f \frac{a_{p,c0} v_{n,c0} + a_{p,c1} v_{n,c1}}{a_{p,c0} + a_{p,c1}} + d_f ((p_{c0} + (\nabla p)_{c0} \cdot \vec{r}_0) - (p_{c1} + (\nabla p)_{c1} \cdot \vec{r}_1)) = \hat{J}_f + d_f (p_{c0} + p_{c1}) \quad (13)$$

Where \vec{F} is the force vector, I is the identity matrix, $\vec{\tau}$ is the stress tensor. J_f is the mass flux, $v_{n,c0}, v_{n,c1}$ are normal velocities, and p_{c0}, p_{c1} are the pressures.

2.2 Pressure Velocity Coupling

2.2.1 SIMPLE Algorithm

The SIMPLE technique was employed to force mass conservation and generate the pressure field p^* , which exploits a correlation between pressure and velocity modification. A predicted pressure p was used to solve the momentum equation, and the resulting face flow $j f^*$ was estimated using the discretized continuity eq. 13.

$$j_f^* = \hat{j}_f + d_f (p_{c0}^* + p_{c1}^*)$$

Subsequently, a modification j'_f was added to the face flux J_f^*

$$j_f = j_f^* + j'_f \quad (14)$$

The SIMPLE algorithm requires j'_f may be calculated as

$$j'_f = d_f (p'_{c0} + p'_{c1}) \quad (15)$$

Where p' = pressure cell correction

To get discrete eq. for the pressure modification p' , the SIMPLE algorithm insert the flux modification eqs.14, 15 in to the discrete continuity eq. 9.

$$a_p p' = \sum_{nb} a_{nb} p'_{nb} + b \quad (16)$$

where $b = \sum_f^{N_{faces}} J_f^* A_f$

To solve the pressure correction, an algebraic multigrid technique might be used. The face flux and cell pressure are corrected after getting a solution.

$$p = p^* + \alpha_p p' \quad (17)$$

$$J_f = J_f^* + d(p'_{c0} - p'_{c1})$$

During each iteration, the pressure relaxation factor (α_p) and the corrected face flow were used to solve the discrete continuity equation.

2.3 Lift and drag forces

The reaction force of a liquid operating on the wing is generated by a flexible flow pattern around the wing portion. When a lift is generated, the air beneath the wing is usually more significant than atmospheric pressure, while the air beneath is generally lower. This pressure differential permits air to flow from the upper wing's root. The following is an analysis of the lift and drag force.

$$F_L = \frac{1}{2} C_L \rho A u^2 \quad (18)$$

$$F_D = \frac{1}{2} C_D \rho A u^2 \quad (19)$$

Where C_L and C_D are the lift and drag coefficient, A, ρ, u are cross-sectional area, density, and velocity respectively.

3. Boundary conditions

This study applied four boundaries to the 2D domain at the bottom, top, right, and left, as shown in fig. 2. The entrance flow was set to a constant velocity (0.14607) [7], and the output flow was set to the right side, with no gradient. To reduce the influence of the boundary condition, the top and bottom boundaries should be placed far enough away from the airfoil.

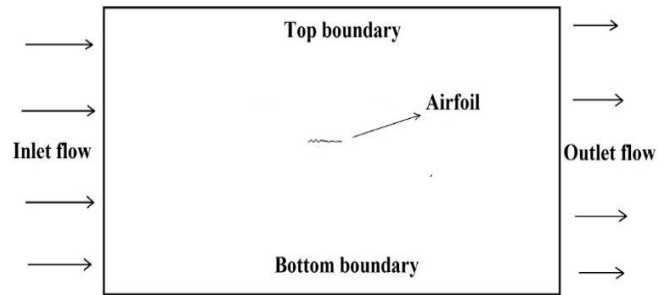


Figure 2: Boundary conditions

4. Results and Discussion

4.1 Effect of Reynolds number and angle of attack

The effect of AOA and Re numbers on airfoil performance is essential to examine. Because it had ramifications for how these wings may function for MAVs of varied sizes, this phrase is also necessary for the use of such wings in MAVs. As a result, a numerical analysis of the effects of the AOA and Re numbers on the aerodynamic performance of airfoils was conducted. Table 1 shows that when the AOA increases from 0 to 10° degrees, the mean lift coefficient increases while the

coefficient of drag drops, resulting in improved propulsive performance. We attempt to maintain a consistent lift with the best lift to drag ratio in any aircraft vehicle. The gliding ratio increased monotonically as the AOA increased at all Reynolds numbers. The drag formation has some exciting outcomes. Because the viscous effect is more common at low Re numbers, leading skin friction to be the significant contribution to drag reduction, the average drag coefficient in each example

drops as the AOA increases, as expected. The shear drag distribution of the pleated airfoil was significantly more complicated due to the complexity of the airfoil design. There are notably significant shear drag maxima on both the pressure and suction surfaces around the top of the corrugation. However, the formation of a large zone of negative shear drag in the superseding gaps is intriguing.

Table 1: Values of C_L and C_D at different Reynolds Number (Re) and at different AOA

Reynolds Number	Angle of attack	C_L	C_D	C_L/C_D	Steady/Unsteady
1000	0	0.1710	0.352	0.484	Steady
	5	0.794	0.2803	2.83	Steady
	10	0.946	0.256	3.68	Steady
1250	0	0.185	0.240	0.771	Steady
	5	0.724	0.173	4.18	Unsteady
	10	0.810	0.162	4.99	Unsteady
1500	0	0.215	0.148	1.45	Steady
	5	0.940	0.094	9.96	Unsteady
	10	1.0453	0.0771	13.55	Unsteady

As a result, the pleated airfoil's low shear drag is due to that negative shear region, which cancels out the influence of the positive shear drag in the different areas of the airfoil. Examining the mean flow over the airfoil exposes the cause of the negative and positive shear drag peaks. The drag coefficient reduces as the Re Number grows, but the lift coefficient increases first and subsequently drops, as shown in table 1.

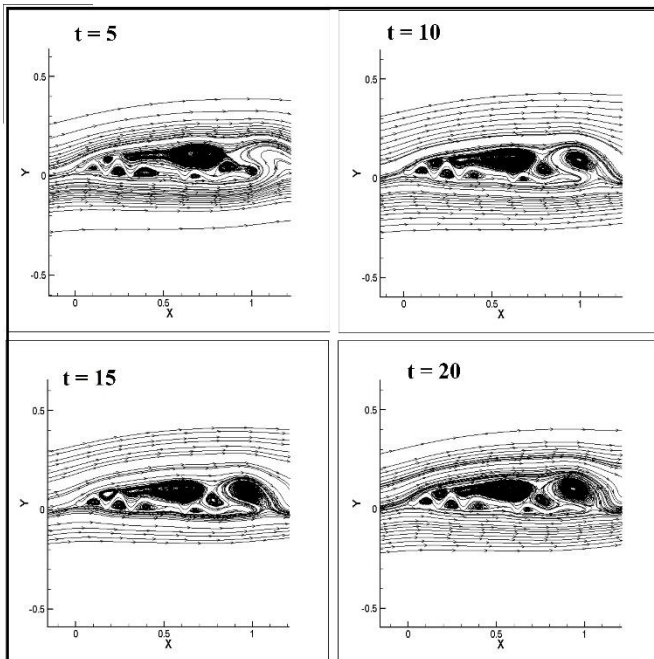


Figure 3: Streamlines at different time units illustrating of the pleated airfoil at $Re=1500$ and $\alpha = 0^\circ$

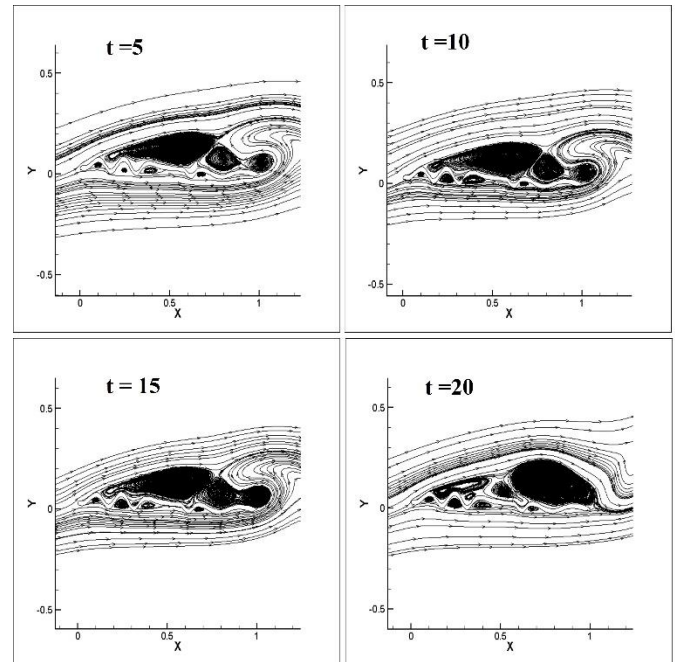


Figure 4: Streamlines at different time units illustrating of the pleated airfoil at $Re=1500$ and $\alpha = 5^\circ$

The source of the negative and positive shear drag peaks is revealed by analyzing the average flow across Aeshna Cyanea's airfoil. The streamline on the pleated airfoil at Reynold Number 1250 displays a trapped vortex in each chamber, as illustrated in fig. 3-5. Different writers [22-24] made the same observation, expecting fluid flow to behave due to the trapped vortex in each hole [25]. Furthermore, the flow separation downstream of each corrugation's tip is reconstituted just upstream of the next corrugation's tip. The flow area between reattachment and detachment has formed recirculating flow with negative shear drag. Additionally, the

negative and positive shear drag maxima arise at the flow recirculation zone, as illustrated in fig. 6, because these locations have a significant surface average gradient in the tangential velocity.

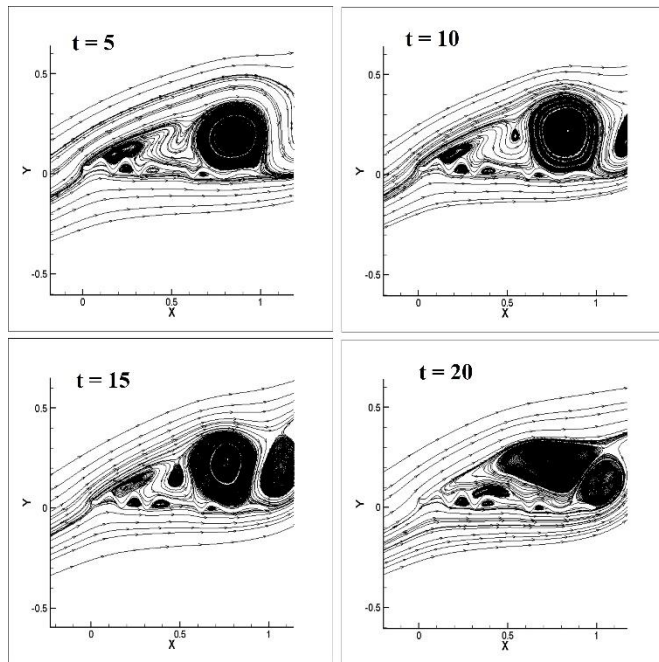


Figure 5: Streamlines at different time units illustrating of the pleated airfoil at $Re=1500$ and $\alpha = 10^\circ$

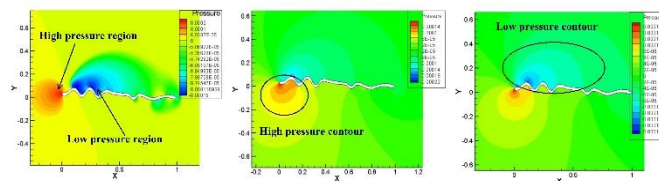


Figure 6: Pressure distribution of pleated airfoil (a) $Re=1000$, (b) $Re=1250$, (c) $Re=1500$

This is similar to the findings [7, 26], which show that pleats increase negative pressure on the upper surface of the airfoil, resulting in increased lift output. Fig. 6 shows pressure contours as a function of AOA and Re numbers. However, the pressure connection on the lower surface of the existing profile was not included in this analysis [27]. We determined that the upper side pressure of the airfoil is always negative, but the lower side pressure is always positive. The trapped vortices reduce stress on the corrugated top airfoil's surface, leading to enhanced lift generation.

5. Conclusions

The numerical simulation of a dragonfly wing airfoil was successfully investigated and observed that as the AOA grows from 0 to 10° , the mean coefficient of lift increases while the coefficient of drag drops, resulting in improved propulsive performance as AOA increases. In each scenario, the average drag coefficient decreases as the AOA increases because

viscous effects are more prevalent at low Re numbers, causing skin friction to be the primary contributor to total drag reduction. The negative and positive shear drag maxima arise in the flow recirculation zone because this is where the tangential velocity has a significant average surface gradient. The pleats produce negative pressure on the upper surface of the airfoil, enhancing lift creation. At the same time, the trapped vortices decrease pressure on the corrugated top surface of the airfoil, thus increasing lift generation.

References

- [1] M Okamoto, K Yasuda, A Azuma, Aerodynamic characteristics of the wings and body of a dragonfly, *Journal of experimental biology*, 199(2), 281-294, 1996.
- [2] Syed Fahad Anwer, Intesaaf Ashraf, Husain Mehdi, Akhlaq Ahmad, Grafi H, On the Aerodynamic Performance of Dragonfly Wing Section in Gliding Mode, *Advances in Aerospace Science and Applications*, 3(3), 227-234, 2013.
- [3] Vargas A, Mittal R, Dong H (2008) A computational study of the aerodynamic performance of a dragonfly wing section in gliding flight, *Bioinspiration & Biomimetics* 3 (2), 026004. <https://doi.org/10.1088/1748-3182/3/2/026004>.
- [4] Wakeling J M and Ellington C P 1997a Dragonfly flight: I. Gliding flight and steady-state aerodynamic forces *J. Exp. Biol.* 200 543-56.
- [5] Newman, B. G., Savage, S. B., and Schouella, D., "Model Test on a Wing Section of a Aeschna Dragonfly", *Scale Effects in Animal Locomotion*, edited by T. J. Pedley, London Academic Press, 1977, pp. 445-477.
- [6] Azuma, A. and Watanabe, T., "Flight Performance of a Dragonfly," *Journal of Experimental Biology*, Vol. 137, 1988, pp. 221-252.
- [7] Husain Mehdi, Brajesh Kumar Lakhera and Anil Kamboj, Numerical Analysis of Steady and Unsteady Flow for Dragonfly Wing Section in Gliding Mode, *International Journal of Advanced Mechanical Engineering*, 4 (4), 365-370, 2014.
- [8] H Song, G Y He, Q Wang, L S Chen, Numerical Study on the Aerodynamic Performance of the Rigid and Corrugated Forewing of Dragonfly in Flapping Flight, *IOP Conf. Series: Materials Science and Engineering* 816 (2020) 012005.
- [9] Rajabi H., Shafiei A., Darvizeh A., Dirks J.-H., Appel E. and Gorb S. N. Effect of microstructure on the mechanical and damping behaviour of dragonfly wing veins, *Royal society open science*, 2016, 3160006160006, <http://doi.org/10.1098/rsos.160006>.
- [10] Michael Bauerheim, Vincent Chapin, Route to chaos on a dragonfly wing cross section in gliding flight, *Physical Review E* 102, 011102(R) (2020).
- [11] Husain Mehdi, Fahad Anwer, Akhlaque Ahmad, Fluid Structure Interaction of Flow around a Pleated Insect 2D Airfoil at Ultra Low Reynolds Numbers, *International Journal of Research in Aeronautical and Mechanical Engineering*, 3(3), 19-37, 2015.
- [12] Husain Mehdi, Sayed Fahad Anwer, Akhlaque Ahmad, Vibration Analysis of Dragonfly wing section in Gliding Mode at Low Reynolds Numbers, *International Journal of Research in Aeronautical and Mechanical Engineering*, 2 (12), 11-22, 2014.
- [13] Wootton R J 1991 The functional morphology of the insect wings of Odonata *Adv. Odonatol.* 5 153-69.
- [14] Newman, D. J. S. and Wootton, R. J., "An Approach to the Mechanics of Pleating in Dragonfly Wings," *Journal of Experimental Biology*, 125, 1986, pp. 361-372.
- [15] Wootten, R. J., "Functional Morphology of Insect Wings," *Annual Review of Entomology*, Vol. 37, 1992, pp. 113-140.
- [16] Engels T, Wehmann H-N, Lehmann F-O. 2020 Three-dimensional wing structure attenuates aerodynamic efficiency in flapping fly wings. *J. R. Soc. Interface* 17: 20190804. <http://dx.doi.org/10.1098/rsif.2019.0804>.
- [17] Chao Wang, Rui Zhang, Chaoying Zhou, Zhenzhong Sun, Numerical Investigation on Flapping Aerodynamic Performance of Dragonfly Wings in Crosswind, *International Journal of Aerospace Engineering*, 2020, <https://doi.org/10.1155/2020/7325154>.

- [18] A. J. Chorin, "Numerical solution of navier-stokes equations", *Mathematics of Computation*, 22:745-762, 1968.
- [19] T. J. Barth and D. Jespersen, "The design and application of upwind schemes on unstructured meshes", Technical Report AIAA-89-0366, AIAA 27th Aerospace Sciences Meeting, Reno, Nevada, 1989.
- [20] D. G. Holmes and S. D. Connell, "Solution of the 2D Navier-Stokes Equations on Unstructured Adaptive Grids", Presented at the AIAA 9th Computational Fluid Dynamics Conference, June, 1989.
- [21] R. D. Rauch, J. T. Batira, and N. T. Y. Yang, "Spatial Adaption Procedures on Unstructured Meshes for Accurate Unsteady Aerodynamic Flow Computations", Technical Report AIAA-91-1106, 1991.
- [22] Rees C J C 1975b Aerodynamic properties of an insect wing section and a smooth airfoil compared *Nature* 258 141–152.
- [23] Newman B G, Savage S B and Schouella D 1977 Model test on a wing section of a Aeschna dragonfly Scale Effects in Animal Locomotion ed T J Pedley (London: Academic) pp 445–77.
- [24] Rudolph R 1977 Aerodynamic properties of *Libellula quadrimaculata* L. (Anisoptera: Libellulidae), and the flow around smooth and corrugated wing section models during gliding flight *Odonatologica*, 7, 49–58.
- [25] Husain Mehdi, Shwetanshu Gaurav, Mudit Sharma, Numerical investigation of fluid flow and aerodynamic performance on a 2D NACA-4412 airfoil, *International Journal of Research in Engineering and Innovation*, 1(1), 1-5, 2017.
- [26] Kesel, A. B., Philippi, U. and Nachtigall, W., "Biomechanical Aspects of Insect Wings – An Analysis using the Finite Element Method," *Computers in Biology and Medicine*, Vol. 28, 1998, pp. 423–437.
- [27] Kesel A B 2000 Aerodynamic characteristics of dragonfly wing sections compared with technical aerofoil, *Journal of Experimental Biology*, 203, 3125–3135

Cite this article as: Sarvesh Kumar, Husain Mehdi, Piyush Gupta, Aerodynamic performance of the dragonfly wing section in gliding mode at ultra-low Reynold number, *International journal of research in engineering and innovation (IJREI)*, vol 6, issue 5 (2022), 321-326. <https://doi.org/10.36037/IJREI.2022.6504>.